

Article

Insight into the Effect of Anionic–Anionic Co-Doping on BaTiO₃ for Visible Light Photocatalytic Water Splitting: A First-Principles Hybrid Computational Study

Souraya Goumri-Said ¹  and Mohammed Benali Kanoun ^{2,*} 

¹ Physics Department, College of Science and General Studies, Alfaisal University, P.O. Box 50927, Riyadh 11533, Saudi Arabia

² Department of Mathematics and Sciences, College of Humanities and Sciences, Prince Sultan University, P.O. Box 66833, Riyadh 11586, Saudi Arabia

* Correspondence: mohammedbenali.kanoun@gmail.com or mkanoun@psu.edu.sa

Abstract: In this research, we thoroughly studied the electronic properties and optical absorption characteristics with double-hole coupling of anions–anion combinations for designing effective photocatalysts for water redox using first-principles methods within the hybrid Heyd–Scuseria–Ernzerhof (HSE06) exchange–correlation formalisms. The findings reveal that the values of formation energy of both the anion mono- and co-doped configurations increase monotonically as the chemical potential of oxygen decreases. The N–N co-doped BaTiO₃ exhibits a more favorable formation energy under an O-poor condition compared with other configurations, indicating that N and N pairs are more likely to be synthesized successfully. Interestingly, all the co-doping configurations give a band gap reduction with suitable position for oxygen production and hydrogen evolution. The obtained results demonstrate that all the co-doped systems constitute a promising candidate for photocatalytic water-splitting reactions. Furthermore, the enhanced ability of the anionic-anionic co-doped BaTiO₃ to absorb visible light and the positions of band edges that closely match the oxidation-reduction potentials of water suggest that these configurations are viable photocatalysts for visible-light water splitting. Therefore, the wide-band gap semiconductor band structures can be tuned by double-hole doping through anionic combinations, and high-efficiency catalysts for water splitting using solar energy can be created as a result.

Keywords: anionic–anionic co-doping; BaTiO₃; Heyd–Scuseria–Ernzerhof (HSE06); photocatalytic water splitting



Citation: Goumri-Said, S.; Kanoun, M.B. Insight into the Effect of Anionic–Anionic Co-Doping on BaTiO₃ for Visible Light Photocatalytic Water Splitting: A First-Principles Hybrid Computational Study. *Catalysts* **2022**, *12*, 1672. <https://doi.org/10.3390/catal12121672>

Academic Editor: John Vakros

Received: 8 November 2022

Accepted: 13 December 2022

Published: 19 December 2022

Publisher's Note: MDPI stays neutral with regard to jurisdictional claims in published maps and institutional affiliations.



Copyright: © 2022 by the authors. Licensee MDPI, Basel, Switzerland. This article is an open access article distributed under the terms and conditions of the Creative Commons Attribution (CC BY) license (<https://creativecommons.org/licenses/by/4.0/>).

1. Introduction

The search for new renewable and clean energy sources has drawn considerable attention in recent years, owing to the increasing serious environmental challenges rooted in fossil fuel usage and resource depletion [1]. One of the most competitive methods for providing a cheap and ecologically acceptable energy source is photocatalytic hydrogen synthesis from water reduction, which can be considered a clean and sustainable strategy for resolving energy problems [1–3]. A variety of photocatalysts based on oxide materials have received extensive attention in research because of their strong photocatalytic activity, nontoxicity, and chemical stability [4]. Among them, Barium titanate (BaTiO₃) is a common ferroelectric compound with a perovskite structure and large band gap of 3.0–3.3 eV [5]. The most crucial feature is that it has the appropriate band positions to split water into hydrogen and oxygen [6–10]. This means that the valence band (VB) and conduction band (CB) edges of BaTiO₃ are in the suitable positions, which satisfies the thermodynamic condition for the water-splitting reaction [5]. The ultraviolet part of the solar energy spectrum, which makes up only 5% of it, has fewer practical applications due to the high band gap of this material. It is conventionally known that more than 45% of solar irradiance is visible light.

Therefore, to enhance visible-light photocatalytic performance, it is crucial to design active photocatalysts that operate in this region. Doping impurity elements into crystal lattices is a common and effective method for modifying the electronic structure and band gap position in semiconductors.

Numerous studies [11–21] have recently used the doping of metal and non-metal elements into semiconductors to change the optoelectronic properties. For instance, experimental research by Upadhyay et al. [12] shows that adding 2.0% Fe to BaTiO₃ results in a noticeable improvement in photocurrent density and a decreasing in band gap because Fe 3d states exist within the band gap region. Nageri and Kumar [13] suggested that Mn-doped BaTiO₃ illustrated higher visible-light-driven photocatalytic activity, which was primarily caused by the energy states connected to the dopants and oxygen vacancies. Demircivi et al. synthesized a W-doped BaTiO₃ nanocomposite photocatalyst and observed that it was more effective in degrading tetracycline than both undoped and highly doped BaTiO₃ at lower doping levels. This may be because less electron-hole recombination occurs [14]. It has also been demonstrated that Rh-doped BaTiO₃, which can produce H₂ from water through a photocatalytic process, has two absorption bands in the visible-light spectrum [15]. Recently, Pie et al. investigated the photocatalytic properties of Mo in BaTiO₃, indicating that doping with 4d metal Mo achieved band-to-band visible-light absorption and showed a striking rise in hydrogen-generation efficiency in contrast to the pristine material [16]. In comparison to the undoped BaTiO₃, Cao et al. [17] discovered that BaTiO₃ doped with anionic N had a lower band gap and increased activity of photo-degradation to Rhodamine-B under irradiation within the visible region, mostly because the valence bandwidth was widened.

On the theoretical side, it has been indicated that doping with various metal impurities modifies the crystal structures and electronic properties of cubic BaTiO₃ [18]. It has also been reported that by substituting a metal dopant at Ba or Ti site into a BaTiO₃ lattice, the electronic nature and impurity ionic size have a direct effect on the stability and the formation of oxygen vacancies [18]. According to the computed results published by Yang et al. [19], band gap energy of BaTiO₃ may be reduced and hole mobility increased by replacing Ti with main group elements including metal (Mo, Tc, Ru, Pd) and transition metal (Cr, Mn, Fe, Co, Ni) atoms. Our previous studies indicated that the electronic structures of BaTiO₃ have been modified by doping rare earth into either Ba or Ti sites using first-principles calculations [20,21]. Recently, Huang et al. [22] reported the effect of doping chalcogens at O site into BaTiO₃ on optical absorption and photocatalytic water splitting. They discovered that the presence of the p-energy state of dopants at the minimum of CB results in the reducing of the band gap and the improvement of the visible range.

Mono-doping, which is the process of adding cations or anions to semiconductors, typically results in the generation of dopant states within the band gap, which could operate as the recombination site for photo-generation of charge carriers and lower photocatalytic activity. This will destroy the photocatalytic activity of photocatalysts. Co-doping with metal cations and anions in large band gap semiconductors has garnered much interest as a solution to these issues [22–24].

Separating photogenerated holes and electrons is made easier by the compensated nature of co-doping with a cation-anion pair, which also passivates the dopants bands and lowers the band gap to a reasonable value [25,26]. As a result, donor-acceptor pairs such as transition metal (MT = V, Nb, Ta, Mo, and W) and anion (X = N, C) atoms are typically used to adjust the band gap of semiconductor-based photocatalysts like TiO₂ [27–30], SrTiO₃ [30,31], NaNbO₃ [32,33], KNbO₃ [34], La₂Ti₂O₇ [35], and BaTiO₃ [36,37]. In addition to cation-anion co-doping, double-hole co-doping has become a successful approach for modifying the band gap of photocatalysts based on perovskite such as SrTiO₃, NaTaO₃, and KNbO₃ [38–40]. The band gap is greatly minimized as a result of anionic-anionic co-doping, which also produces completely occupied delocalized intermediate states above the valence region, while increasing the overall stability [41].

In this study, we investigated the impact of double-hole-mediated coupling on the electronic structures and the photocatalytic water-splitting performance of BaTiO₃ by performing hybrid density functional theory (DFT) computations. By analyzing the geometrical crystal structures, energies of formation, electronic properties, and optical absorption characteristics of anion mono- and co-doped BaTiO₃, we distinctly demonstrate that anion-anion (N–N, C–S, N–P, and P–P) coupling combinations can successfully reduce the band gap by adding an intermediate filled and delocalized state and can also produce attractive band alignments that are suitable for photo-electrochemical water splitting. This type of double-hole-mediated co-doping, for example, is a successful way to modify the band structures of a large band gap photocatalyst and then improve the performance of the photocatalytic ability of photocatalysts, including visible-light water splitting.

2. Computational Details

The Quantum Atomistix ToolKit (QuantumATK) software package, which is based on the local integration of the atomic orbitals method and density functional theory (DFT), was used to perform the reported computations [42]. The exchange and correlation energy functionals have been expressed using the Perdew–Burke–Ernzerhof generalized gradient approximation [43]. The pseudopotential of norm-conserving PseudoDojo was used to define the interaction between ion nuclei and valence electrons [44]. Self-consistent field simulations with a tolerance limit of 10^{−8} Ha were used to determine energy convergence. PseudoDojo-medium was chosen as the basis set, and a mesh cut-off energy of 90 Ha was used. A force on each atom was reduced to 0.05 eV/Å by minimizing the total energy of the system using the Broyden–Fletcher–Goldfarb–Shanno (LBFGS) approach, which led to the stable arrangement of the atoms and the lattice parameters. A 4 × 4 × 3 and 10 × 10 × 8 Monkhorst–Pack [45] k-grid was used for the Brillouin Zone integration in performing geometry optimization and electronic calculations. The accurate band gap energy and optical properties of semiconductors were predicted using the Heyd–Scuseria–Ernzerhof (HSE06) more precise hybrid density functional [46,47]. Short-range (*sr*) and long-range (*lr*) components of the exchange and correlation energy in the HSE function were defined as:

$$E_{xc}^{HSE}(\mu, \alpha) = \alpha E_x^{HF, sr, \mu} + (1 - \alpha) E_x^{PBE, sr, \mu} + E_x^{PBE, lr, \mu} + E_c^{PBE} \quad (1)$$

where μ denotes the parameter defining the range separation of Coulomb kernel ($\mu = 0.2/\text{Å}$), α is the mixing parameter of 0.25, and E_x and E_c represent the exchange and correlation contributions, respectively.

3. Results and Discussion

In the pristine cubic BaTiO₃ structure, Ba atoms are situated at the eighth apexes of the cube corner, Ti atoms occupy the center of the octahedron, and O atoms are located at the face centers, forming a symmetric octahedron (TiO₆), as illustrated in Figure 1. The computed lattice parameters and Ba–O (2.85) and Ti–O (2.02) bond lengths are in good agreement with the experimental measurements [48] and values of previous theoretical studies [20,21,36,49]. The electronic band structure and density of state (DOS) were computed using HSE06 functional, as shown in Figure 1. The obtained direct band gap of 3.0 eV is more compatible with both experimental results [5] and previous reported results [20,21,36,49]. The analysis of the DOS figure shows that the VB and CB edges principally consist of O 2*p* states and Ti 3*d* states, respectively. Nevertheless, the absence of any Ba electronic states around the maximum valence edge and lowest conduction edge suggests that Ba merely contributes to the structure of BaTiO₃ and has no impact on the electronic structure close to the Fermi level.

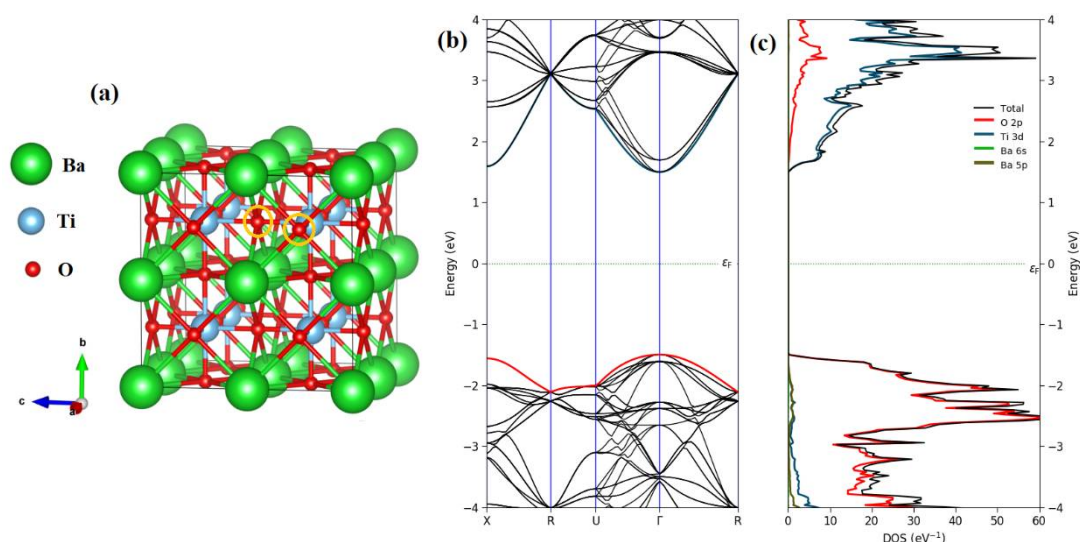


Figure 1. (a) The optimized supercell structure of $2 \times 2 \times 2$ supercell and (b) calculated band structure and total and partial DOS of pristine BaTiO₃. (Ba in green, Ti in light blue, O in red, orange circles of doping atoms).

For mono- and co-doped systems, a $2 \times 2 \times 2$ supercell approach is adopted with periodic boundary conditions, consisting of 8 Ba, 8 Ti, and 24 O atoms. The anionic mono-doped configuration is modeled by replacing one of the anion dopants (N, P, C, S) with one of the O atoms in the BaTiO₃ supercell. It has been discovered that the anionic–anionic co-doped BaTiO₃ system, which is constructed by utilizing two anionic dopants to substitute the two nearby O atoms at the same level, marked with orange circles in Figure 1, is more stable than others [38–40]. In this case, we look only at this particular lowest-energy design. The lattice constants of the modified systems are gathered in Table 1. For all co-doping systems, the lattice constants of the relaxed structures decreased due to the incorporation of an anionic element.

Table 1. The optimized lattice parameters, and the formation of energy for pristine and mono- and co-doped BaTiO₃.

	a (Å)	b (Å)	c (Å)	E_b (eV)	E_f (eV)	
					Ti-Rich	O-Rich
Pure	8.005	8.005	8.005	-	-	-
N	8.014	8.014	8.014	-	-10.10	-2.75
C	8.008	8.008	8.073	-	-5.33	-0.08
S	8.070	8.064	8.423	-	-4.31	0.94
P	8.012	8.012	8.232	-	-2.08	3.18
N–N	8.088	8.015	8.088	1.317	-17.53	-6.23
C–S	8.267	8.017	8.107	2.179	-11.89	-1.32
N–P	8.297	8.024	8.086	3.038	-13.12	-2.62
P–P	8.321	7.980	8.321	4.637	-8.79	1.72

To investigate the relative stability of co-doped configurations, we determined the binding energy (E_b) by adopting the following relation:

$$E_b = E_{A1} - E_{A2} - E_{pure} + E_{A1+A2} \quad (2)$$

where E_{pure} , E_{A1} , E_{A2} , and E_{A1+A2} are the total energies of pure, (first anion, A1) mono-doped, (second anion A2) mono-doped, and (double-hole, A1 + A2) co-doped BaTiO₃, respectively. The calculated values of binding energy are gathered in Table 1. The computed

binding energy values are positive for the investigated double-hole co-doped systems, which contribute to its stability relative to the analogous mono-doped systems.

To determine the best growth circumstances for different doped configurations, we computed the formation energy, E_f , using the following equation [50,51]

$$E_f = E_{doped} - E_{undoped} - n_X\mu_X + n_O\mu_O \quad (3)$$

where $E_{undoped}$ and E_{doped} denote the total energies of the pure and doped BaTiO₃ supercell. The number n represents the addition or subtraction of dopant and host ions. The chemical potential of the X (N, P, S, C) and O atoms are denoted by the symbols μ_X , and μ_O , respectively, and depend on the parameters of the experiment. The formation energy is dependent on the chemical potentials of the host atoms represented by the environment because defects occur in response to the experimental growth or annealing process. As a stable structure, the chemical potentials of the BaTiO₃ and the constituent Ba, Ti, and O atoms should satisfy the following expression:

$$\mu_{Ba} + \mu_{Ti} + 3\mu_O = \mu_{BaTiO_3} \quad (4)$$

where μ_{Ba} is computed from the total energy of one atom of Ba in bulk crystal structure. For Ti-rich conditions, the μ_{Ti} can be obtained in the ground state with energy of bulk Ti and μ_O estimated according to the Expression (4). Under O-rich conditions, μ_O is determined as the total energy of O₂ molecules. The variable μ_X is the energy of a single X atom inside a cube with a side length of 10 Å. The calculated energies of formation for anionic mono- and co-doped are summarized in Table 1 as well as illustrated in Figure 2. It reveals that a larger negative value of formation energy illustrates a thermodynamically more favorable co-doping procedure. The findings imply that the formations of all configurations are conceptually beneficial because of the negative formation energy. The analysis in Figure 2 shows that N mono-doping is proven to be more advantageous than in other mono-doping cases, a result which can be ascribed to the similar radii of atoms. In addition, the values of formation energy of anion mono-doping rise when the μ_O varies from O-poor and O-rich environments. This shows that this type of doping is easily formed under O-poor conditions. It is found that anionic co-doping has much lower formation energy than the comparable mono-doping, which is energetically favorable in O-poor conditions. This is mainly owing to the stronger interaction between anionic and anionic atoms in the former. It should be noted that N–N-co-doped BaTiO₃ exhibits a more favorable energy of formation compared with the other configurations, indicating that N and N combinations are more likely to be synthesized successfully.

Next, we investigated the impact of anion mono-doping on the electronic structures of BaTiO₃. In the case of anionic mono-doping, the overall electron number may increase or decrease in comparison to that of a pristine BaTiO₃, in which spin-polarization calculations are performed to handle these mono-doped systems. For N-mono-doped BaTiO₃, as an N-dopant contains one less valence electron compared with an O atom, the N-doping is one electron deficient. This is reflected in asymmetrical DOSs with regard to the electrons in the spin-up and spin-down channels, as displayed Figure S1, exhibiting a magnetic nature with total magnetic moment of +1.0 μ_B . This is principally coming from the N atom (+0.954 μ_B). When the N impurity substitutes the O atom, one acceptor level in the band gap is generated. These unfilled states superior to the Fermi level are extremely unfavorable for photocatalytic activity, as a result of their ability to trap charge carriers and speed up the electron-hole combination procedure. The photocatalytic performance may be impacted by the partially filled impurity levels near the Fermi level, which could serve as an electron-hole recombination junction. For P-mono-doped BaTiO₃, replacing one O atom with one P impurity will also result in the formation of a single acceptor, because the P atom has one less valence electron than O atoms. P-doping introduces localized levels that arise in the majority and minority spin channel. Therefore, an additional hole was formed in the system which was followed by a spin-polarization effect. These

results show a magnetic behavior. Moreover, the total magnetic moment obtained is $1.0 \mu_B$, primarily due to the P atom ($0.904 \mu_B$). Below the Fermi level, there are several occupied localized states that mostly result from the combining of P $3p$ and O $2p$ states. Additionally, it is discovered that a number of empty dopant states, primarily caused by P- $3p$ localized states, exist close to the minimum of CB. For C-doping, the introduction of two acceptor levels into the BaTiO_3 lattice results from the substitution of O with C. The total magnetic moment of C-doping of $+2.002 \mu_B$ is determined by spin-resolved calculations, which originates mainly from the C atom with local moment of $(+1.741 \mu_B)$. At the maximum valence band, it is evident that a number of dopant states, largely composed of C- $2p$ orbitals, are present. Surprisingly, above the Fermi level, no unoccupied localized dopant states are visible. The absence of uninhabited localized bands above the Fermi level is mentioned. It also has a narrow effective band gap of 2.22 eV, making it a reasonable photocatalyst for the visible region. In the case of S-doping, the S atom has the same number of valence electrons as O atoms and, as a result, the interaction between S $3p$ states and Ti $3d$ states occurs when one S atom replaces one O atom. As can be observed from the DOS shown in Figure S2, there appear to be occupied localized bands above the valence region that are generated by S $3p$ states and O $2p$ states, whereas the minimum CB is made up of Ti states. Without empty localized states arising beyond the Fermi level, the band gap is found to be 2.24 eV, which is advantageous for the absorption of visible light.

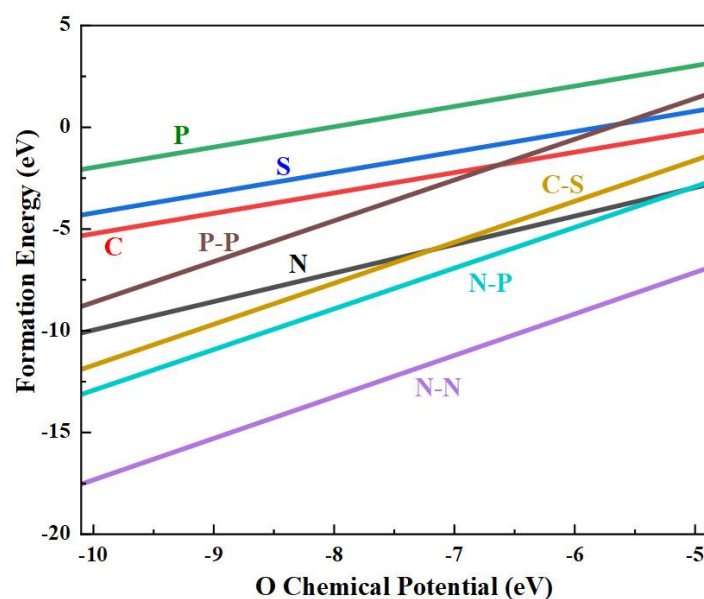


Figure 2. Estimated energies of formation in respect to the oxygen chemical potential for anionic mono- and anionic-anionic co-doped configurations.

BaTiO_3 mono-doped with anionic elements, as demonstrated above, produces certain impurity states within the band gap, thus narrowing the gap region. These in-gap states have certain drawbacks for photocatalytic water splitting since they could serve as sites for the capture and recombination of photo-generated electrons and holes, which would reduce the efficiency of photon conversion. In fact, the double-hole-mediated anionic co-doping of BaTiO_3 with N–N, C–S, N–P, and P–P atom combinations may compensate for the charge without the formation of unfilled bands above the Fermi level. In N–N co-doped systems, the replacement of two near-neighboring O atoms by two N-dopants introduces two net holes and a new N–N bond is created in which the bond length distance is 1.518 Å. The obtained value is much shorter than that of the distance of 2.830 Å between two O atoms for the pristine BaTiO_3 , indicating the strong coupling between the two N atoms. The band structure and DOS are calculated to study the impact of N–N co-doping on the electronic characteristics of BaTiO_3 , as shown in Figure 3a. The HSE06 calculation predicts a band

gap of 1.55 eV that is notably lower than the pure compound owing to the existence of the intermediate states located above the valence band. Additionally, since no acceptor states are seen beyond the Fermi level, the recombination effects will be lower than they would be in an N mono-doped system. Note that two completely occupied states are created within the band gap after the N–N co-doping. According to the PDOS, the edge of the VB of N–N co-doped configuration is mainly contributed to by O 2*p* states, whereas the edge of the CB is dominated by Ti 3*d* states.

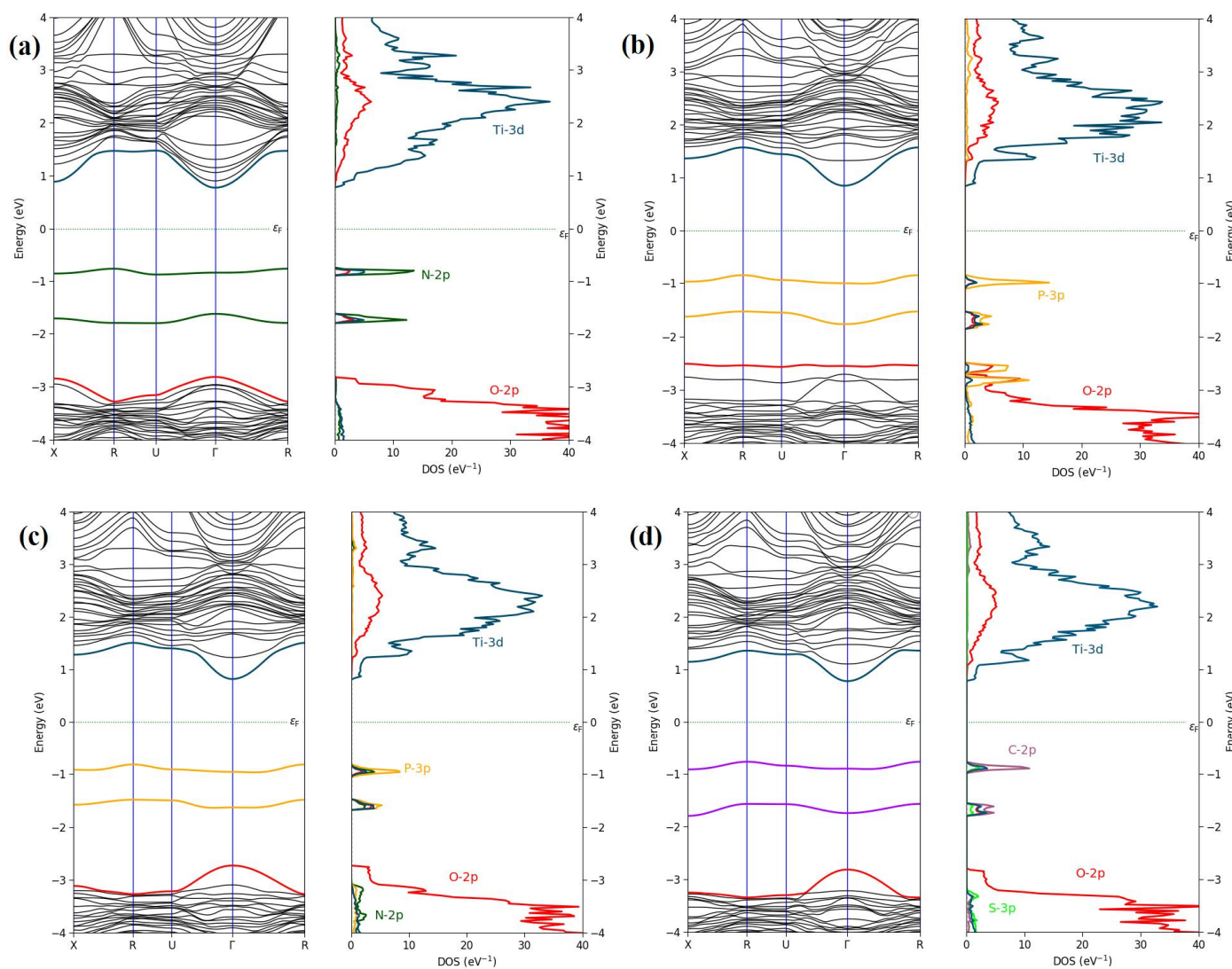


Figure 3. Electronic band structure and partial density of states for (a) N–N, (b) P–P, (c) N–P, and (d) C–S co-doped BaTiO₃.

Most filled-in gap states are situated above the VB as a result of the strong mixture between the Ti 3*d*, and N 2*p* states, as well as the strong coupling between the O 2*p* states. Additionally, no acceptor states can be seen above the Fermi level, proving that there will be significantly fewer recombination sites than in the case of N mono-doping. Thus, these unoccupied dopants states that manifest in the mono-doping system can be eliminated by such double-hole N–N co-doping. The P–P co-doping into BaTiO₃ is nearly identical to the N–N co-doping, because it likewise has two net holes. The P–P bond distance is found to be 2.109 Å. The analysis in Figure 3b shows that the edges of VB and CB are predominantly composed of the P 3*p* states and Ti 3*d* states, respectively. When two P atoms are in close proximity to one another, the unpaired 3*p* electrons of the two neighboring

P atoms hybridize with one another and create a bonding band and an anti-bonding band, since each of the P atoms has one unpaired electron. The latter hybridization introduces three completely occupied sub-bands above the VB edge, while the anti-bonding state is situated near the minimum of CB. Interestingly, there is no unfilled impurity states in the band gap region. The calculated band gap of P–P co-doping is found to be 1.70 eV, which would undoubtedly increase the visible radiation photocatalysis and decrease the recombination losses. For N–P co-doped BaTiO₃, co-doping with N and P introduces two net holes, one from the N atom and the other from the P atom. The DOS of the co-doping configuration is shown in Figure 3c, in which fully occupied states appear just above the maximum of VB, so no unoccupied localized states are between the VB and CB edges. Therefore, the band gap is reduced due to 1.64 eV. The N–P bond length obtained is 1.79 Å. Additionally, above the maximum of VB, completely filled dopant states are produced by the admixture of N 2*p*, P 3*p*, and O 2*p* states. This also represents a reliable link between the N 2*p* and P 3*p* states caused by double holes.

We also investigated the C–S co-doping in a BaTiO₃ supercell. The geometry optimization shows that the C–S bond length distance is found to be 1.85 Å, which is much shorter than that of O–O (2.85 Å, proving the strong coupling between C and S atoms). According to the PDOS displayed in Figure 3d, completely occupied states are produced above the upper limit of VB, reducing the band gap to 1.55 eV. Moreover, the maximum of VB consists of O 2*p* states and the lower limit of CB is made up of Ti 3*d* states. Unlike the N–N co-doping, the C atom is responsible for the two holes. All localized states between the borders of VB and CB are occupied as the bonding state moves into the VB and the anti-bonding state moves towards the CB. Moreover, there are two occupied states, primarily originated from C 2*p* and S 3*p* states that are located above the VB edge.

Insightful, and closely connected to the electronic structure of materials are optical functions. For the ongoing design of enhanced semiconductor applications, in-depth knowledge of absorption coefficient and refractive index dispersions is necessary. The depth to which light at a given wavelength (energy) traverses a material before being absorbed is defined by the absorption coefficient, which provides information about the optimal efficiency of energy conversion. In Figure 4, we plotted the absorption spectra versus wavelength (from 0 to 800 nm) for BaTiO₃ and the doped derivatives configurations to see the impact of the band gap narrowing on the optical response to photon absorption. According to an investigation of optical absorption characteristics, pure BaTiO₃ can accumulate only in the UV area, appearing at one peak as $\lambda = 345$ nm, and has no response to visible-light absorption. The anionic-anionic co-doping extends the absorption coefficient leading to the appearance of more peaks compared to that of the pure BaTiO₃. These rising peaks are known as absorption edges. The optical absorption spectrum of the P–P doping system shows three peaks, the first one at 290 nm and the second one at $\lambda = 370$ nm, in which the most interesting peak appears in the blue zone of the visible spectrum at $\lambda = 470$ nm but with less intensity compared to the former peaks. The C–S doping configuration is more interesting as it shows a redshift of the BaTiO₃ spectra with four peaks in the visible ranges at 388 nm, 425 nm, 513 nm, and 590 nm, the reasonably highest absorption intensity being 4.25×10^5 (cm⁻¹). The N–P co-doping shows a peak in absorption with an intensity of 6.1×10^5 (cm⁻¹) in the start of the violet wavelength (380 nm) and two more peaks at blue and green wavelengths. The N–N co-doping produces two peaks in blue and green wavelengths with 2.82×10^5 (cm⁻¹) absorption intensity. We can relate this different behavior to the band gap already calculated in Figure 4. In practice, at low frequencies, free carriers are connected to the primary electronic conduction mechanism in a semiconductor. As the photon energy increases and gets closer to the energy gap, a new conduction mechanism may emerge. An inter-band transition occurs when an electron is excited by a photon from an occupied state in the valence band to an unoccupied state in the conduction band. We anticipate that inter-band transition will have a threshold energy at the energy gap. The frequency dependence of the absorption coefficient for direct allowed transitions is governed by the following formula: $\alpha_{\text{abs}}(\omega) \propto \frac{1}{\omega} \sqrt{\hbar\omega - E_g}$. As a result, a threshold at the energy

gap E_g determines the direct optically permitted inter-band transitions in our materials. As a result, there are many different physical processes with a different frequency dependence of $\alpha_{\text{abs}}(\omega)$. In some cases, using the imaginary part of the dielectric function, given by $\varepsilon_2(\omega) = \frac{\hbar c}{\omega} \alpha_{\text{abs}}(\omega)$, to describe absorption is preferable, where \tilde{n} denotes the index of refraction. Furthermore, the absorption coefficient of an indirect inter-band transition in which a phonon is absorbed is: $\alpha_{\text{abs}}(\omega) = C_a \frac{(\hbar\omega - E_g + \hbar\omega_q)^2}{\exp(\hbar\omega_q/k_B T) - 1}$, where C_a is a constant for the phonon absorption process, $\hbar\omega_q$ is phonon energy, and k_B represents the Boltzmann constant ($8.380649 \text{ J K}^{-1} \text{ mol}^{-1}$).

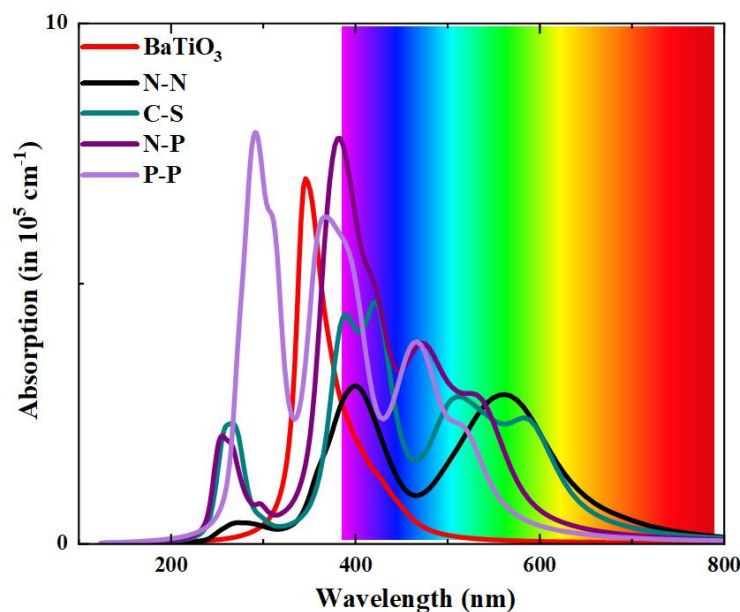


Figure 4. Calculated optical absorption spectra for pristine and anionic-anionic co-doped BaTiO₃ at the HSE06 level.

The determination of the energy-band potentials of photocatalysts is crucial for understanding the photocatalytic mechanism of semiconductor materials, since the energy-band potentials of semiconductor-based photocatalysts are closely connected to the redox potential of photogenerated charge carriers. The respective locations of VB and CB potentials of pristine BaTiO₃ can be computed through the expression [5]:

$$E_{CB} = \chi - 0.5E_g + E_0 \quad (5)$$

$$E_{VB} = E_{CB} + E_g \quad (6)$$

where E_g represents the band gap calculated using HSE06 functional, χ is the absolute electronegativity, and E_0 is the hydrogen dimension's free-electron energy ($\sim 4.5 \text{ eV}$). For pure BaTiO₃, the CB edge is found to be 0.385 eV larger than the reduction potential, and the VB edge is 0.89 eV smaller than the oxidation potential, indicating good agreement with previous work [36]. It indicates that while pure BaTiO₃ is very effective at splitting water, it can absorb only UV light, which reduces the efficiency of its photocatalytic activity. The alignments of the band edge of pure BaTiO₃ are shown in Figure 5 with respect to the redox potentials of water [40]. According to the findings of the band alignment, the designed co-doping systems have the capacity to thermodynamically split water because the CB and VB edge locations of N-N, P-P, N-P, and C-S co-doped BaTiO₃ are situated outside the redox potential of water. This demonstrates that both the photo-reduction and the photo-oxidation of water are beneficial processes in this system. Therefore, anionic co-doped BaTiO₃ materials would make good water-splitting candidates when exposed to visible light.

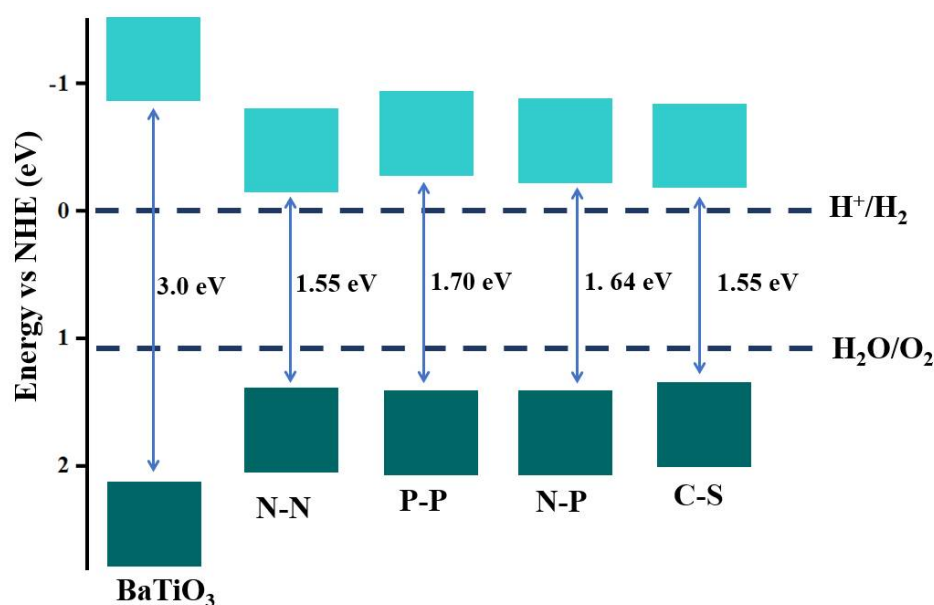


Figure 5. The calculated VB and CB edge energy levels versus normal hydrogen electrode (NHE) using HSE06 functional of N–N, P–P, N–P, and C–S co-doped BaTiO₃.

4. Conclusions

We performed hybrid density functional calculations to thoroughly examine the crystal geometry electronic structures and optical properties of anionic mono-doped and anionic-anionic co-doped BaTiO₃ in order to generate efficient water redox photocatalysts. According to our findings, most of the co-doping systems can successfully lower the formation energy of the associated mono-doped system. Therefore, co-doping configurations are suitable under O-rich conditions. It was found that the formation energies of all the co-doped systems and anionic mono-doped systems increase monotonically as the chemical potential of O rises. Moreover, the anionic co-doping combinations (N–N, P–P, N–P, and C–S) generate completely filled dopant states in the band gap region, resulting in a reduction in the effective band gaps. It was also revealed that the double-hole anionic co-doped BaTiO₃ is proven to be a successful absorber of visible light by the computed optical absorption curves. Additionally, the locations of the band edges in relation to the redox potentials of water demonstrate that anionic co-doping pairs can meet the needs of H₂ and O₂ generation. According to these findings, combining anionic co-doping pairs via double holes is an efficient method for tuning the band gap of wide-band gap semiconductors, and for creating very effective catalysts for water splitting of solar light.

Supplementary Materials: The following supporting information can be downloaded at: <https://www.mdpi.com/article/10.3390/catal12121672/s1>. Figure S1. Calculated total and partial DOS of (a) N doped, (b) P doped, (c) C doped and (d) S doped BaTiO₃. Here, the vertical dashed line denotes the Fermi level. Figure S2. Side view of the optimized structures of (a) pristine, (b) N–N, (c) C–S, (d) N–P and (e) P–P co-doped BaTiO₃.

Author Contributions: Conceptualization, S.G.-S. and M.B.K.; methodology, S.G.-S. and M.B.K.; software, S.G.-S. and M.B.K.; validation, S.G.-S. and M.B.K.; formal analysis, S.G.-S. and M.B.K.; investigation, S.G.-S. and M.B.K.; resources, S.G.-S. and M.B.K.; data curation, S.G.-S. and M.B.K.; writing—original draft preparation, S.G.-S. and M.B.K.; writing—review and editing, S.G.-S. and M.B.K.; visualization, S.G.-S. and M.B.K.; supervision, S.G.-S. and M.B.K.; project administration, S.G.-S. and M.B.K. All authors have read and agreed to the published version of the manuscript.

Funding: This research received no external funding.

Data Availability Statement: Data sharing is not applicable to this article.

Conflicts of Interest: The authors declare no conflict of interest.

References

1. Kudo, A.; Miseki, Y. Heterogeneous photocatalyst materials for water splitting. *Chem. Soc. Rev.* **2009**, *38*, 253–278. [[CrossRef](#)] [[PubMed](#)]
2. Byrne, C.; Subramanian, G.; Pillai, S.C. Recent advances in photocatalysis for environmental applications. *J. Environ. Chem. Eng.* **2018**, *6*, 3531–3555. [[CrossRef](#)]
3. Moniz, S.J.A.; Shevlin, S.A.; Martin, D.J.; Guo, Z.X.; Tang, J.W. Visible-light driven heterojunction photocatalysts for water splitting—A critical review. *Energy Environ. Sci.* **2015**, *8*, 731–759. [[CrossRef](#)]
4. Wang, Q.; Domen, K. Particulate Photocatalysts for Light-Driven Water Splitting: Mechanisms, Challenges, and Design Strategies. *Chem. Rev.* **2020**, *120*, 919–985. [[CrossRef](#)] [[PubMed](#)]
5. Xu, Y.; Schoonen, M.A. The absolute energy positions of conduction and valence bands of selected semiconducting minerals. *Am. Miner.* **2000**, *85*, 543–556. [[CrossRef](#)]
6. Maeda, K. Rhodium-Doped Barium Titanate Perovskite as a Stable p-Type Semiconductor Photocatalyst for Hydrogen Evolution under Visible Light. *ACS Appl. Mater. Interfaces* **2014**, *6*, 2167–2173. [[CrossRef](#)]
7. Zhang, S.; Chen, D.; Liu, Z.; Ruan, M.; Guo, Z. Novel strategy for efficient water splitting through pyro-electric and pyro-photo-electric catalysis of BaTiO₃ by using thermal resource and solar energy. *Appl. Catal. B Environ.* **2021**, *284*, 119686. [[CrossRef](#)]
8. Gao, C.; Yu, H.; Zhang, L.; Zhao, Y.; Xie, J.; Li, C.; Cui, K.; Yu, J. Ultrasensitive Paper-Based Photoelectrochemical Sensing Platform Enabled by the Polar Charge Carriers-Created Electric Field. *Anal. Chem.* **2020**, *92*, 2902–2906. [[CrossRef](#)]
9. Zhou, Z.; Tang, H.X.; Sodano, A.H. Vertically Aligned Arrays of BaTiO₃ Nanowires. *ACS Appl. Mater. Interfaces* **2013**, *5*, 11894–11899. [[CrossRef](#)]
10. Fang, T.; Hu, H.; Liu, J.; Jiang, M.; Zhou, S.; Fu, J.; Wang, W.; Yang, Y. Type-II Band Alignment Enhances Unassisted Photoelectrochemical Water-Splitting Performance of the BaTiO₃/CdS Ferroelectric Heterostructure Photoanode under Solar Light Irradiation. *J. Phys. Chem. C* **2021**, *125*, 18734–18742. [[CrossRef](#)]
11. Fernandes, E.; Gomes, J.; Martins, R.C. Semiconductors Application Forms and Doping Benefits to Wastewater Treatment: A Comparison of TiO₂, WO₃, and g-C₃N₄. *Catalysts* **2022**, *12*, 1218. [[CrossRef](#)]
12. Upadhyay, S.; Shrivastava, J.; Solanki, A.; Choudhary, S.; Sharma, V.; Kumar, P.; Singh, N.; Satsangi, V.R.; Shrivastav, R.; Waghmare, U.V.; et al. Enhanced photoelectrochemical response of BaTiO₃ with Fe doping: Experiments and first-principles analysis. *J. Phys. Chem. C* **2011**, *115*, 24373–24380. [[CrossRef](#)]
13. Nageri, M.; Kumar, V. Manganese-doped BaTiO₃ nanotube arrays for enhanced visible light photocatalytic applications. *Mater. Chem. Phys.* **2018**, *213*, 400–405. [[CrossRef](#)]
14. Demircivi, P.; Simsek, E.B. Visible-light-enhanced photoactivity of perovskite-type W-doped BaTiO₃ photocatalyst for photodegradation of tetracycline. *J. Alloys Compd.* **2019**, *774*, 795–802. [[CrossRef](#)]
15. Cui, Y.; Sun, H.; Shen, G.; Jing, P.; Pu, Y. Effect of Dual-Cocatalyst Surface Modification on Photodegradation Activity, Pathway, and Mechanisms with Highly Efficient Ag/BaTiO₃/MnO_x. *Langmuir* **2020**, *36*, 498–509. [[CrossRef](#)]
16. Xie, P.; Yang, F.; Li, R.; Ai, C.; Lin, C.; Lin, S. Improving hydrogen evolution activity of perovskite BaTiO₃ with Mo doping: Experiments and first-principles analysis. *Int. J. Hydrogen Energy* **2019**, *44*, 11695–11704. [[CrossRef](#)]
17. Cao, J.; Ji, Y.; Tian, C.; Yi, Z. Synthesis and enhancement of visible light activities of nitrogen-doped BaTiO₃. *J. Alloys Compd.* **2014**, *615*, 243–248. [[CrossRef](#)]
18. Sharma, V.; Pilania, G.; Rossetti, G.A.; Slenes, K.; Ramprasad, R. Comprehensive examination of dopants and defects in BaTiO₃ from first principles. *Phys. Rev. B Condens. Matter Mater. Phys.* **2013**, *87*, 134109. [[CrossRef](#)]
19. Yang, F.; Yang, L.; Ai, C.; Xie, P.; Lin, S.; Wang, C.; Lu, X. Tailoring Bandgap of Perovskite BaTiO₃ by Transition Metals Co-Doping for Visible-Light Photoelectrical Applications: A First-Principles Study. *Nanomaterials* **2018**, *8*, 455. [[CrossRef](#)]
20. Alshoaibi, A.; Kanoun, M.B.; Haq, B.U.; AlFaify, S.; Goumri-Said, S. Ytterbium doping effects into the Ba and Ti sites of perovskite barium titanate: Electronic structures and optical properties. *Results Phys.* **2020**, *18*, 103257. [[CrossRef](#)]
21. Alshoaibi, A.; Kanoun, M.B.; Haq, B.U.; AlFaify, S.; Goumri-Said, S. Insights into the Impact of Yttrium Doping at the Ba and Ti Sites of BaTiO₃ on the Electronic Structures and Optical Properties: A First-Principles Study. *ACS Omega* **2020**, *5*, 15502–15509. [[CrossRef](#)] [[PubMed](#)]
22. Huang, H.-C.; Yang, C.-L.; Wang, M.-S.; Ma, X.-G. Chalcogens doped BaTiO₃ for visible light photocatalytic hydrogen production from water splitting. *Spectrochim. Acta Part A* **2019**, *208*, 65–72. [[CrossRef](#)]
23. Ohno, T.; Tsubota, T.; Nakamura, Y.; Sayama, K. Preparation of S, C cation-codoped SrTiO₃ and its photocatalytic activity under visible light. *Appl. Catal. A Gen.* **2005**, *288*, 74–79. [[CrossRef](#)]
24. Niu, M.; Cheng, D.; Cao, D. Enhanced photoelectrochemical performance of anatase TiO₂ by metal-assisted SeO coupling for water splitting. *Int. J. Hydrogen Energy* **2013**, *38*, 1251–1257. [[CrossRef](#)]
25. Yang, K.; Dai, Y.; Huang, B. Review of First-Principles Studies of TiO₂: Nanocluster, Bulk, and Material Interface. *Catalysts* **2020**, *10*, 972. [[CrossRef](#)]
26. Zhang, J.; Tse, K.; Wong, M.; Zhang, Y.; Zhu, J. A brief review of co-doping. *Front. Phys.* **2016**, *11*, 117405. [[CrossRef](#)]
27. Gai, Y.; Li, J.; Li, S.-S.; Xia, J.-B.; Wei, S.-H. Design of Narrow-Gap TiO₂: A Passivated Codoping Approach for Enhanced Photoelectrochemical Activity. *Phys. Rev. Lett.* **2009**, *102*, 036402. [[CrossRef](#)]

28. Kanoun, M.B.; Alshoaibi, A.; Goumri-Said, S. Hybrid Density Functional Investigation of Cu Doping Impact on the Electronic Structures and Optical Characteristics of TiO₂ for Improved Visible Light Absorption. *Materials* **2022**, *15*, 5645. [[CrossRef](#)]
29. Ikram, M.; Ul-Haq, M.A.; Haider, A.; Haider, J.; Ul-Hamid, A.; Shahzadi, I.; Bari, M.A.; Ali, S.; Goumri-Said, S.; Kanoun, M.B. The enhanced photocatalytic performance and first-principles computational insights of Ba doping-dependent TiO₂ quantum dots. *Nanoscale Adv.* **2022**, *4*, 3996–4008. [[CrossRef](#)]
30. Niishiro, R.; Kato, H.; Kudo, A. Nickel and either tantalum or niobium-codoped TiO₂ and SrTiO₃ photocatalysts with visible-light response for H₂ or O₂ evolution from aqueous solutions. *Phys. Chem. Chem. Phys.* **2005**, *7*, 2241–2245. [[CrossRef](#)]
31. Wang, J.; Wang, Y.; Wang, Y.; Zhang, X.; Fan, Y.; Liu, Y.; Yi, Z. Role of P in improving V-doped SrTiO₃ visible light photocatalytic activity for water splitting: A first—Principles study. *Int. J. Hydrogen Energy* **2021**, *46*, 20492–20502. [[CrossRef](#)]
32. Wang, B.; Kanhere, P.D.; Chen, Z.; Nisar, J.; Pathak, B.; Ahuja, R. Anion-doped NaTaO₃ for visible light photocatalysis. *J. Phys. Chem. C* **2013**, *44*, 22518–22524. [[CrossRef](#)]
33. Wang, G.-Z.; Chen, H.; Wu, G.; Kuang, A.-L.; Yuan, H.-K. Hybrid Density Functional Study on Mono- and Codoped NaNbO₃ for Visible-Light Photocatalysis. *ChemPhysChem* **2016**, *17*, 489. [[CrossRef](#)]
34. Maarouf, A.A.; Gogova, D.; Fadlallah, M.M. Metal-doped KNbO₃ for visible light photocatalytic water splitting: A first principles investigation. *Appl. Phys. Lett.* **2021**, *119*, 063901. [[CrossRef](#)]
35. Liu, P.; Nisar, J.; Pathak, B.; Ahuja, R. Cationic–anionic mediated charge compensation on La₂Ti₂O₇ for visible light photocatalysis. *Phys. Chem. Chem. Phys.* **2013**, *15*, 17150–17157. [[CrossRef](#)]
36. Fo, Y.; Ma, Y.; Dong, H.; Zhou, X. Tuning the electronic structure of BaTiO₃ for an enhanced photocatalytic performance using cation–anion codoping: A first-principles study. *New J. Chem.* **2021**, *45*, 8228. [[CrossRef](#)]
37. Fo, Y.; Zhou, X. A theoretical study on tetragonal BaTiO₃ modified by surface co-doping for photocatalytic overall water splitting. *Int. J. Hydrogen Energy* **2022**, *47*, 19073–19085. [[CrossRef](#)]
38. Liu, P.; Nisar, J.; Pathak, B.; Ahuja, R. Hybrid density functional study on SrTiO₃ for visible light photocatalysis. *Int. J. Hydrogen Energy* **2012**, *16*, 11611–11617. [[CrossRef](#)]
39. Wang, J.; Teng, J.; Pu, L.; Huang, J.; Wang, Y.; Li, Q. Double-hole-mediated coupling of anionic dopants in perovskite NaNbO₃ for efficient solar water splitting. *Int. J. Quantum Chem.* **2019**, *119*, e25930. [[CrossRef](#)]
40. Wang, G.; Huang, Y.; Kuang, A.; Yuan, H.; Li, Y.; Chen, H. Double-Hole-Mediated Codoping on KNbO₃ for Visible Light Photocatalysis. *Inorg. Chem.* **2016**, *55*, 9620–9631. [[CrossRef](#)]
41. Wang, J.; Huang, J.; Meng, J.; Li, Q.; Yang, J. Single- and few-layer BiOI as promising photocatalysts for solar water splitting. *Phys. Chem. Chem. Phys.* **2016**, *18*, 17517. [[CrossRef](#)]
42. Smidstrup, S.; Markussen, T.; Vanraeyveld, P.; Wellendorff, J.; Schneider, J.; Gunst, T.; Verstichel, B.; Stradi, D.; Khomyakov, P.A.; Vej-Hansen, U.G.; et al. QuantumATK: An integrated platform of electronic and atomic-scale modelling tools. *J. Phys. Condens. Matter* **2020**, *32*, 015901. [[CrossRef](#)] [[PubMed](#)]
43. Perdew, J.P.; Burke, K.; Ernzerhof, M. Generalized gradient approximation made simple. *Phys. Rev. Lett.* **1996**, *77*, 3865. [[CrossRef](#)] [[PubMed](#)]
44. Van Setten, M.; Giantomassi, M.; Bousquet, E.; Verstraete, M.; Hamann, D.; Gonze, X.; Rignanese, G.-M. The PseudoDojo: Training and grading a 85 element optimized norm-conserving pseudopotential table. *Comput. Phys. Commun.* **2018**, *226*, 39–54. [[CrossRef](#)]
45. Monkhorst, H.J.; Pack, J.D. Special points for Brillouin-zone integrations. *Phys. Rev. B* **1976**, *13*, 5188. [[CrossRef](#)]
46. Ferreira, L.G.; Marques, M.; Teles, L.K. Approximation to density functional theory for the calculation of band gaps of semiconductors. *Phys. Rev. B* **2008**, *78*, 125116. [[CrossRef](#)]
47. Kanoun, M.B.; Goumri-Said, S.; Schwingenschlögl, U.; Manchon, A. Magnetism in Sc-doped ZnO with zinc vacancies: A hybrid density functional and GGA+U approaches. *Chem. Phys. Lett.* **2012**, *532*, 96–99. [[CrossRef](#)]
48. Ravel, B.; Stern, E.A.; Vedrinskii, R.I.; Kraizman, V. Local structure and the phase transitions of BaTiO₃. *Ferroelectrics* **1998**, *206*, 407–430. [[CrossRef](#)]
49. Chakraborty, A.; Liton, M.N.H.; Sarker, M.S.I.; Rahman, M.M.; Khan, M.K.R. A comprehensive DFT evaluation of catalytic and optoelectronic properties of BaTiO₃ polymorphs. *Phys. B Condens. Matter* **2023**, *648*, 414418. [[CrossRef](#)]
50. Janotti, A.; van de Walle, C.G. Native point defects in ZnO. *Phys. Rev. B* **2007**, *76*, 165202. [[CrossRef](#)]
51. Kanoun, M.B. Vacancy defects- and strain-tunable electronic structures and magnetism in two-dimensional MoTe₂: Insight from first-principles calculations Surf. *Interfaces* **2021**, *27*, 101442. [[CrossRef](#)]